

# Ising nematic quantum critical point in a metal: a Monte Carlo study

Yoni Schattner,<sup>1,\*</sup> Samuel Lederer,<sup>2,\*</sup> Steven A. Kivelson,<sup>2</sup> and Erez Berg<sup>1</sup>

<sup>1</sup>*Department of Condensed Matter Physics, The Weizmann Institute of Science, Rehovot, 76100, Israel*

<sup>2</sup>*Department of Physics, Stanford University, Stanford, CA 94305, USA*

(Dated: June 22, 2022)

The Ising nematic quantum critical point (QCP) associated with the zero temperature transition from a symmetric to a nematic *metal* is an exemplar of metallic quantum criticality. We have carried out a minus sign-free quantum Monte Carlo study of this QCP for a two dimensional lattice model with sizes up to  $24 \times 24$  sites. The system remains non-superconducting down to the lowest accessible temperatures. The results exhibit scaling behavior over the accessible ranges of temperature, (imaginary) time, and distance. This scaling behavior has remarkable similarities with recently measured properties of the Fe-based superconductors proximate to their putative nematic QCP.

## I. INTRODUCTION

A hallmark of strongly correlated electron systems is the competition of ground states with different kinds of order.[1] In this context, a central set of unsettled theoretical issues concerns the character of quantum critical points (QCPs) in metals [2–4]. Such metallic QCPs have been identified in several heavy fermion compounds[5]; evidence for quantum critical behavior has also been found in the ruthenate  $\text{Sr}_3\text{Ru}_2\text{O}_7$  [6, 7], and the cuprate and iron-based superconductors [8]. Quantum criticality is also often invoked as a possible explanation of the “strange” or “bad” metal behavior seen in a variety of such materials [9–16].

To date, there exists no satisfactory theory of metallic QCPs in  $d = 2$  or 3 spatial dimensions although a number of field theoretic approaches have been attempted [17–34]. Among the unsettled issues are: a) the values of critical exponents, and which properties can be expressed as scaling functions involving these exponents, b) the extent to which metallic QCPs are preempted by superconducting [35–43] or other forms [38, 44, 45] of auxiliary order, that gap out the Fermi surface, c) whether there exists a “non-Fermi liquid” metal in the quantum critical regime. Controlled theoretical methods, that can be used both to benchmark the field theories and for comparison with experiments, are greatly needed. Determinant quantum Monte Carlo (DQMC)[46, 47]—in particular, in cases where the fermion sign problem can be circumvented [48–50]—may serve this purpose. Such methods have been successfully applied in several problems in which critical bosonic fluctuations are coupled to fermions with a Dirac-like dispersion [51–53].

In this paper, we report a DQMC study of a two-dimensional sign problem-free lattice model that exhibits an “Ising nematic” QCP in a metal at finite fermion density; in the nematic phase, the discrete lattice rotational symmetry is spontaneously broken from  $C_4$  to  $C_2$ . This is a particularly relevant QCP given that ne-

matic order [54–59] and nematic quantum critical fluctuations [60–65] have been observed in many of the materials mentioned above.

Our simulations are limited to finite system sizes – up to  $24 \times 24$  lattice sites. Within our numerical accuracy, we find evidence for a continuous nematic quantum phase transition with critical exponents that are significantly different from those of a nematic QCP in an insulator. Specifically, in the disordered phase near the QCP, where the dimensionless quantum control parameter  $h \geq h_c$ , the thermodynamic (zero frequency) nematic two-point correlator (defined in Eq. 5) is consistent with the following functional description:

$$D(h, T, \mathbf{q}, i\omega_n = 0) \approx \left[ \frac{A}{T^\lambda + b(h - h_c) + \kappa|\mathbf{q}|^2} \right]^\gamma \quad (1)$$

where  $T$  is the temperature,  $\mathbf{q}$  is the wave-vector,  $\omega_n$  is

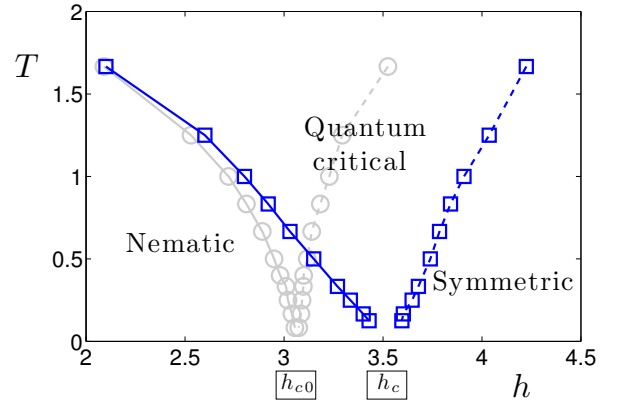


FIG. 1: Phase diagram of the model obtained by DQMC, as a function of the transverse field  $h$  and temperature  $T$ . Here,  $V = t$ ,  $\alpha = 0.5$ ,  $\mu = -0.5t$ . The solid line marks the transition temperature,  $T_N$ , between the nematic and the symmetric phases. The line extrapolates to the  $T = 0$  QCP at  $h_c$ . The dashed line marks  $T_{\text{cross}}$ , where the nematic susceptibility reaches 50% of its magnitude at  $h = h_c \approx 3.525$  at the same temperature. The pale (grey) lines show the corresponding temperatures for the case  $\alpha = 0$  (where the fermions and pseudospins are decoupled). In this case, the QCP occurs at  $h_{c0} \approx 3.06$ .

\*These authors have contributed equally to this work.

the Matsubara frequency, and  $A$ ,  $b$ , and  $\kappa$  are positive dimensionful constants. We find that the exponents in this expression take values  $\lambda = 1.0 \pm 0.1$  and  $\gamma = 1.0 \pm 0.1$ . (See Fig. 8.)

This implies, among other things, that the uniform susceptibility  $\chi \equiv D(h, T, \mathbf{0}, 0)$  has a Curie-Weiss form with an effective Weiss temperature which varies linearly with  $(h_c - h)$ , as can be seen in Fig. 1. Eq. 1 can be viewed as a scaling relation,  $D(h, T, \mathbf{q}, 0) = \xi^{\gamma/\nu} \Phi(x, y)$ , where  $\xi \sim |h - h_c|^{-\nu}$ ,  $x = T\xi^{\tilde{z}}$ ,  $y = |\mathbf{q}|\xi$ . In Eq. 1,  $\gamma$  is the conventionally defined susceptibility exponent, the correlation length exponent  $\nu \equiv \gamma/(2 - \eta)$ , where  $\eta$  is the anomalous dimension of the nematic field, and we have introduced an ‘‘apparent dynamical exponent,’’  $\tilde{z} = (\nu\lambda)^{-1}$ . The values of these exponents derived from our Monte Carlo data are given in Table I.

To illustrate the significance of these exponents, note that working backwards from the exponents corresponding to the  $d + z$  dimensional classical Ising model with dynamical exponent  $z = 1$  (also listed in Table I) would yield  $\lambda = 1.96$ ,  $\gamma = 1.24$ , and  $2 - \eta = 1.96$ . Indeed, we find critical exponents consistent with this expectation by DQMC when we set to zero the coupling between the critical fluctuations and the fermions.

Including results at finite (Matsubara) frequencies, we find a wide intermediate regime where the full dynamical fluctuation spectrum is well described by the simple ‘‘functional approximant’’  $D(h, T, \mathbf{q}, i\omega_n) \approx A(h, T, \mathbf{q}, i\omega_n)$ , where

$$A(h, T, \mathbf{q}, i\omega_n) \equiv \frac{A}{T + b(h - h_c) + \kappa|\mathbf{q}|^2 + c|\omega_n|}. \quad (2)$$

However, in contrast with the thermodynamic correlation function, as shown in Fig. 10, the dynamical response exhibits noticeable deviations from this form for the few lowest values of  $|\mathbf{q}|$ ;  $|\mathbf{q}| \sim 2\pi/L$  where  $L$  is the system width. It is unclear whether these deviations should be dismissed as finite size effects, or taken as indicators of a different form of dynamical scaling closer to criticality, i.e. at lower temperatures and larger system sizes than are presently accessible. Taking Eq. (2) at face value, one finds the dynamical critical exponent  $z \approx 2$ , as would be obtained from a naive dynamical scaling assumption  $\tilde{z} = z$ . This last result is at odds with theoretical expectations, [102] and so requires special analysis, especially given that there are reasons to question the validity of naive dynamical scaling [3, 16].

In the fermionic sector we find results consistent with strongly renormalized Fermi liquid, ‘‘marginal Fermi liquid’’ [66], or weakly non-Fermi liquid behavior down to our lowest temperatures ( $T_{min} \approx 0.02E_F$ , where  $E_F$  is the Fermi energy). In particular, at the QCP, the effective quasiparticle weight,  $Z_{\mathbf{k}_F}(T)$ , defined in terms of the single-fermion Green’s function in Eq. (14), remains substantial. However, it monotonically decreases on cooling, with downward curvature. In a Fermi liquid,  $Z_{\mathbf{k}_F}(T)$  would approach a positive limit as  $T \rightarrow 0$ , while in a weak non-Fermi liquid, it would vanish in proportion to

TABLE I: Critical exponents for a  $2d$  quantum Ising QCP with  $z = 1$  (classical  $3d$  Ising), and for the Ising nematic QCP in a metal from our DQMC simulations. In the limit of vanishing coupling to the fermions, exponents from our DQMC simulations are consistent with  $3d$  classical Ising values.  $\tilde{z}$  is the ‘‘apparent dynamical exponent’’ defined below Eq. (1).

Critical Exponents	$\nu$	$\gamma$	$\eta$	$\tilde{z}$
$2d$ Ising QCP	0.63	1.24	0.04	1.0
$2d$ metallic Ising nematic QCP	$0.5 \pm 0.1$	$1.0 \pm 0.1$	$0.0 \pm 0.3$	$2.0 \pm 0.3$

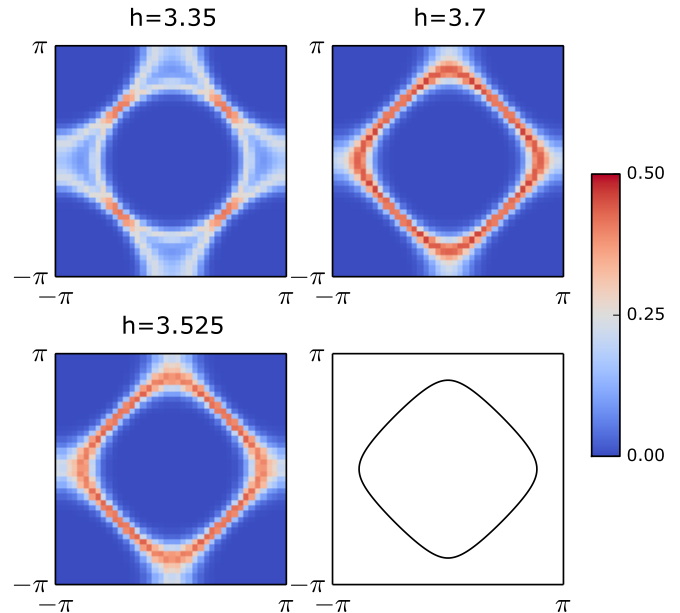


FIG. 2: Fermion Green’s function,  $G(\mathbf{k}, \tau = \beta/2)$ , as a function of momentum  $\mathbf{k}$  across the Brillouin zone for three different values of the transverse field:  $h = 3.35$  (in the nematic phase),  $h = 3.525$  (near the QCP), and  $h = 3.7$  (in the disordered phase). In the nematically ordered phase, the data is averaged over both orientations of the order parameter.  $G(\mathbf{k}, \tau = \beta/2)$  is proportional to the integral over the spectral function  $A(\mathbf{k}, \omega)$  over an energy window of width  $T$  [see Eq. (11)]. The temperature is  $T = 1/8$ , and the system size is  $L = 20$ . The data were taken from systems with either periodic or anti-periodic boundary conditions. The Fermi surfaces are seen as peaks in  $G(\mathbf{k}, \tau = \beta/2)$ . The lower right panel shows the Fermi surface of the bare band structure.

a small power of  $T$ . Fig. 2 shows maps of the low-energy spectral weight as a function of momentum in the disordered phase, at the QCP, and in the ordered phase. The existence[67] of ‘‘cold-spots’’ along the zone diagonals, where the quasiparticles are relatively weakly scattered, is apparent. Finally, no superconducting transition is found down to our lowest temperatures, although the superconducting susceptibility in the s-wave channel is peaked about  $h \approx h_c$ . (See Fig. 13.)

The remainder of the paper is organized as follows: in

Sec. I we define the lattice Hamiltonian and describe its phase diagram; in the next section, we provide evidence for the statements above regarding bosonic correlations (III A), superconductivity (III C), and single-fermion correlations (III D); finally, in Sec. IV, we discuss various caveats concerning the interpretation of our results, and their bearing on both prior theoretical work and the interpretation of experiments.

## II. MODEL AND PHASE DIAGRAM

Our model is illustrated in Fig. 3, and is defined on a two-dimensional square lattice. Every lattice site hosts a single (spinful) fermionic degree of freedom. Each link has a pseudospin-1/2 degree of freedom that couples to the fermion bond-density. The system is described by the following Hamiltonian:

$$H = H_f + H_b + H_{\text{int}}, \quad (3)$$

where

$$\begin{aligned} H_f &= -t \sum_{\langle i,j \rangle, \sigma} c_{i\sigma}^\dagger c_{j\sigma} - \mu \sum_{i, \sigma} c_{i\sigma}^\dagger c_{i\sigma}, \\ H_b &= V \sum_{\langle\langle i,j \rangle\rangle; \langle\langle k,l \rangle\rangle} \tau_{i,j}^z \tau_{k,l}^z - h \sum_{\langle i,j \rangle} \tau_{i,j}^x, \\ H_{\text{int}} &= \alpha t \sum_{\langle i,j \rangle, \sigma} \tau_{i,j}^z c_{i\sigma}^\dagger c_{j\sigma}. \end{aligned} \quad (4)$$

Here,  $c_{j\sigma}^\dagger$  creates a fermion on site  $j$  with spin  $\sigma = \uparrow, \downarrow$ ,  $\langle i, j \rangle$  denotes a pair of nearest-neighbor sites on the square lattice,  $t$  and  $\mu$  are the hopping strength and chemical potential, respectively,  $\tau_{i,j}^a$  ( $a = x, y, z$ ) denote Pauli matrices that act on the pseudospin that lives on the bond connecting the neighboring sites  $i$  and  $j$ ,  $V > 0$  is the nearest-neighbor Ising interaction between neighboring pseudospins (here,  $\langle\langle i, j \rangle\rangle; \langle\langle k, l \rangle\rangle$  denotes a pair of nearest-neighbor bonds),  $h \cdot V$  is the strength of a transverse field that acts on the pseudospins, and  $\alpha$  is the

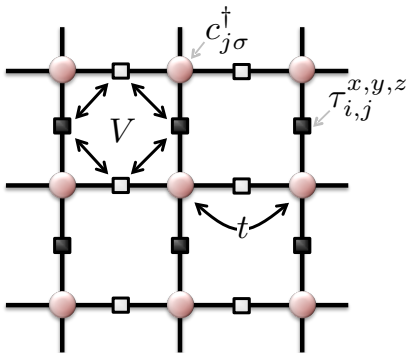


FIG. 3: Illustration of the lattice model (3). Spinful electrons reside on the sites, while the Ising pseudospins live on the bonds. The pseudospins interact with their neighbors antiferromagnetically, and are coupled to the fermion bond density.

dimensionless coupling strength between the pseudospin and the fermion bond density.

The pseudospins are not related to the physical spins of the electrons; their ordering corresponds to a nematic transition. The model (3) should be viewed as an effective lattice model, designed to give a nematic QCP. Microscopically, the nematic degrees of freedom could represent (via Hubbard-Stratonovich transformation) interactions involving the same electrons that form the Fermi surface, or another, independent degree of freedom (such as a phonon mode that becomes soft at a structural transition). So long as the properties of the QCP are universal, the low-energy behavior does not depend on its microscopic origin.

For  $\alpha = 0$ , the system is composed of two decoupled sets of degrees of freedom: free fermions, and pseudospins governed by  $H_b$ , which has the form of a  $d = 2$  transverse field Ising model. At zero temperature, the pseudospins undergo a second-order quantum phase transition from a paramagnet to an “antiferromagnet” that breaks  $90^\circ$  rotational symmetry at  $h = h_{c0}$ . This transition is in the 3 dimensional classical Ising universality class. At  $T = 0$ , the pseudospin degrees of freedom are gapped in both the nematic and isotropic phases. At finite temperatures, a line of second-order classical  $d = 2$  Ising transitions extends from the QCP in the  $h - T$  plane.

For non-zero  $\alpha$ , the phase diagram is similar, but exhibits quantitative and qualitative modifications. Fig. 1 shows the phase diagram, obtained by DQMC, for both  $\alpha = 0$  and  $\alpha \neq 0$ . The  $\alpha \neq 0$  transition between the nematic and isotropic phases remains second order, and extrapolates to a new QCP, shifted relative to  $h_{c0}$ . More striking is the change in the slope with which the phase boundary,  $T_N(h)$ , approaches the QCP. For  $\alpha = 0$ , the slope diverges at low temperature, consistent with the expectation for the transverse field Ising transition, where  $T_N \propto |h - h_{c0}|^{\nu z}$  with  $\nu = 0.63$  and  $z = 1$ . In contrast, for  $\alpha > 0$ , we find that  $T_N \propto (h_c - h)$ . On the disordered side of the transition, we define a crossover line by identifying  $h_{\text{cross}}(T)$  as the value of  $h$  at which the static susceptibility at fixed  $T$  has fallen to half of its value at  $h = h_c$ .  $T_{\text{cross}}(h)$ , the inverse of  $h_{\text{cross}}$ , also vanishes linearly with  $h$  upon approaching the QCP, although its slope is steeper than that of  $T_N(h)$ .

The linear behavior of  $T_N(h)$  for small  $h_c - h$  is also seen for other model parameters. In Fig. 4 we show the phase diagram for two values of the fermion density, controlled by the chemical potential  $\mu$ . As the fermion density is reduced, both  $h_c - h_{c0}$  and the range over which  $T_N(h)$  is linear become smaller, indicating that the effect of the coupling between electrons near the Fermi surface and the nematic modes becomes weaker. The fact that  $T_N(h)$  appears linear at low temperature for both values of fermion density is consistent with this being a *universal* property of the metallic QCP.

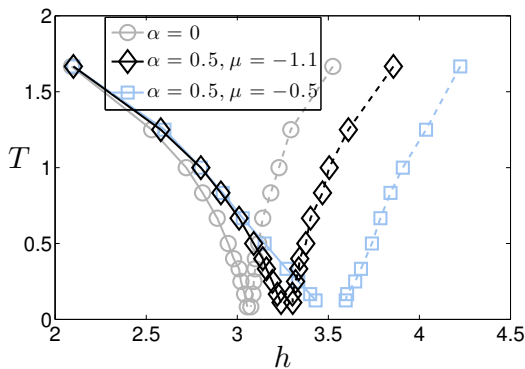


FIG. 4: The phase diagram for several sets of parameters. Gray circles represent the decoupled problem ( $\alpha = 0$ ), while black diamonds and blue squares represent the coupled problem ( $\alpha = 0.5$ ) at 0.6 and 0.8 fermions per site, respectively.

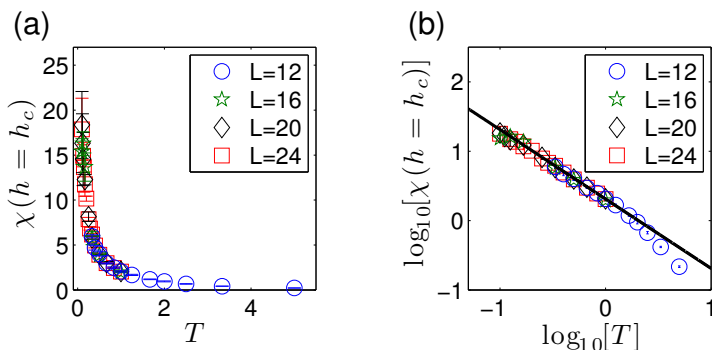


FIG. 5: Nematic susceptibility at the QCP,  $\chi(h = h_c, T)$ , as a function of temperature. Panel a) shows the susceptibility on a linear scale. The same data are displayed on a log-log scale in panel b). The black line is proportional to  $1/T$ .

### III. DQMC RESULTS AND ANALYSIS

We have simulated the Hamiltonian (3) with system sizes between  $L = 8$  and  $L = 24$ , and temperatures between  $0.025t$  and  $5t$ . These simulations do not suffer from the minus sign problem: the fermion determinants obtained from integrating out the spin up and spin down fermions are identical and real, so the product is nonnegative. Near the QCP, global updates of the pseudospin space-time configurations need to be introduced in order to overcome critical slowing down.

Some technical details related to the DQMC simulations are discussed in Appendix A. Here, we shall focus on the results and data analysis. Unless stated otherwise, the model parameters used in the simulations were:  $V = t$ ,  $\alpha = 0.5$ ,  $\mu = -0.5t$ ,  $t = 1$ .

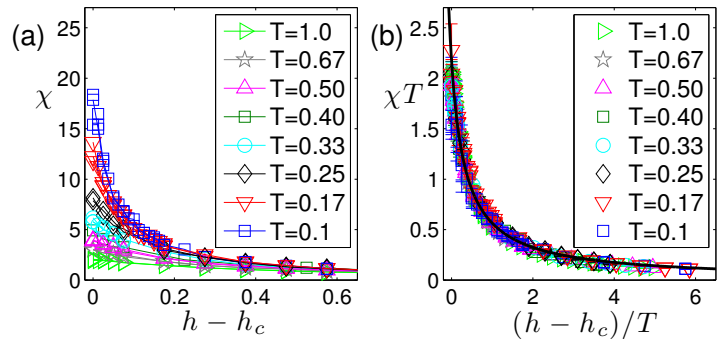


FIG. 6: (a) Nematic susceptibility,  $\chi(h, T)$ , as a function of  $h - h_c$  for a system sizes  $L = 16, 20$ , and  $24$  at various temperatures. (b) The same data, scaled appropriately for  $\lambda = 1$  and  $\gamma = 1$ , collapse on a single curve. The black curve is the function  $F(x) = 2.1/(1 + 2.9x)$ .

#### A. Thermodynamic nematic correlations

The two-point function for the nematic order parameter field is defined as

$$D(h, T, \mathbf{q}, i\omega_n) = \frac{1}{L^2} \sum_{i,j} \int_0^\beta d\tau e^{i\omega_n \tau - i\mathbf{q} \cdot \mathbf{r}_{ij}} \langle N_i(\tau) N_j(0) \rangle. \quad (5)$$

Here,  $\mathbf{r}_{ij} = \mathbf{r}_i - \mathbf{r}_j$ , and the nematic order parameter is defined as  $N_i = \sum_j \eta_{ij} \tau_{ij}^z$ , where  $\eta_{ij} = 1/4$  for  $\mathbf{r}_{ij} = \pm \hat{\mathbf{x}}$ ,  $\eta_{ij} = -1/4$  for  $\mathbf{r}_{ij} = \pm \hat{\mathbf{y}}$ , and  $\eta_{ij} = 0$  otherwise. The phase diagram discussed above was determined using the uniform susceptibility  $\chi(h, T) \equiv D(h, T, \mathbf{0}, 0)$  and standard finite size scaling techniques, described in Appendix B.

Fig. 5 shows  $\chi(h = h_c, T)$ , which diverges upon cooling. Examining the data on a log-log plot, [Fig. 5(b)], the susceptibility is seen to follow a power law,  $\chi(h = h_c, T) = A/T^\lambda$  with  $\lambda \approx 1$ , over more than a decade of temperature between  $0.1V < T \lesssim 2V$ . The slope of  $\log(\chi)$  vs.  $\log(T)$  is independent of the system size for  $L \geq 12$ .

To establish the scaling behavior of  $\chi$  away from  $h_c$ , we plot the susceptibility for different temperatures and system sizes, as a function of  $h - h_c$  [Fig. 6(a)]. For the system sizes displayed ( $16 \leq L \leq 24$ ),  $\chi$  is only weakly dependent on  $L$ . In Fig. 6(b) we plot  $T^\lambda \chi(h, T)$  for  $h > h_c$  as a function of  $(h - h_c)/T^\gamma$ , with  $\lambda = 1.0$  and  $\gamma = 1.0$ . The different curves collapse onto each other, as expected for a scaling function.

Next, we examine the momentum dependence of the static correlator  $D(h, T, \mathbf{q}, i\omega_n = 0)$  near the QCP. Fig. 7 shows  $D^{-1}(h, T, \mathbf{q}, i\omega_n = 0)$  as a function of  $|\mathbf{q}|^2$  for various values of  $h - h_c$  and  $T$ . For small momentum, the momentum dependence consists of an essentially isotropic term, approximately proportional to  $|\mathbf{q}|^2$ . Combined with the form of  $\chi(h, T)$  discussed above, we deduce that the static nematic propagator, for  $h - h_c$  small but positive, is well-described by the functional ap-



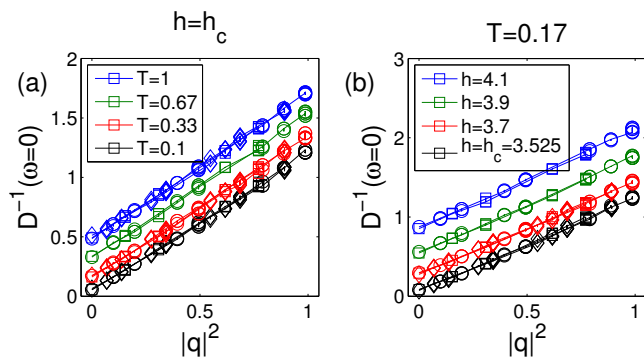


FIG. 7: Quadratic momentum dependence of the inverse propagator at zero frequency. (a) shows  $D^{-1}(\omega=0)$  vs  $|\mathbf{q}|^2$  for all orientations of  $\mathbf{q}$ , at  $h = h_c$  and various temperatures. (b) shows the same for fixed temperature  $T = 0.17t$  and a variety of values of the quantum tuning parameter  $h$ . In each case the momentum dependence remains quadratic. Momenta from multiple system sizes (represented by squares for  $L = 16$ , circles for  $L = 20$ , and diamonds for  $L = 24$ ) fall on the same curve, indicating that the properties shown are in the thermodynamic limit.

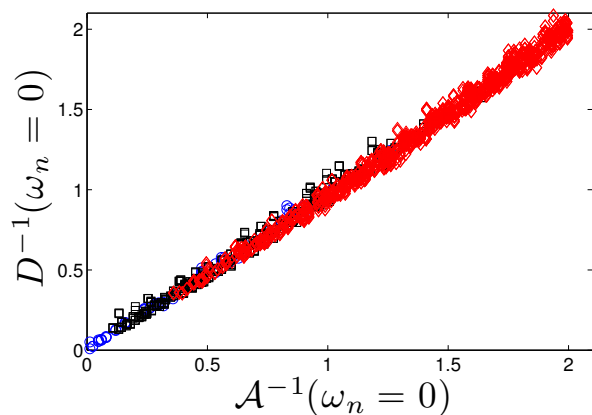


FIG. 8: Comparison between the thermodynamic ( $\omega_n = 0$ ) functional approximant,  $\mathcal{A}$  from Eq. 2, and the nematic correlator,  $D$ . Data shown represent  $L = 16, 20$ , and  $24$ ,  $h = 3.525, 3.7, 3.9$ , and  $4.1$ , and temperatures  $T = 1.0, 0.67, 0.5, 0.33, 0.25, 0.17, 0.13, 0.1, 0.05$ , and  $0.025$ . To exhibit the momentum dependence we have used blue circles for  $\mathbf{q} = \mathbf{0}$  (71 data points), black squares for  $|\mathbf{q}| = (2\pi/L)$  and  $(2\pi/L)\sqrt{2}$  (568 data points), and red diamonds for all other  $\mathbf{q}$  (1916 data points).

proximant of Eq. (2) with  $\omega_n = 0$ ,  $A \approx 2.1$ ,  $b \approx 2.9t$ ,  $\kappa \approx 2.6t$ , and the lattice spacing set to unity. This is explicitly demonstrated in Fig. 8.

## B. Dynamic nematic correlations

The dependence of  $D$  on Matsubara frequency,  $\omega_n = 2\pi Tn$ , is shown in Fig. 9. At intermediate  $\omega_n$  ( $0.5t \lesssim \omega_n \lesssim 2t$ ) and for  $\mathbf{q} \neq \mathbf{0}$ ,  $D^{-1}$  is an approximately linear

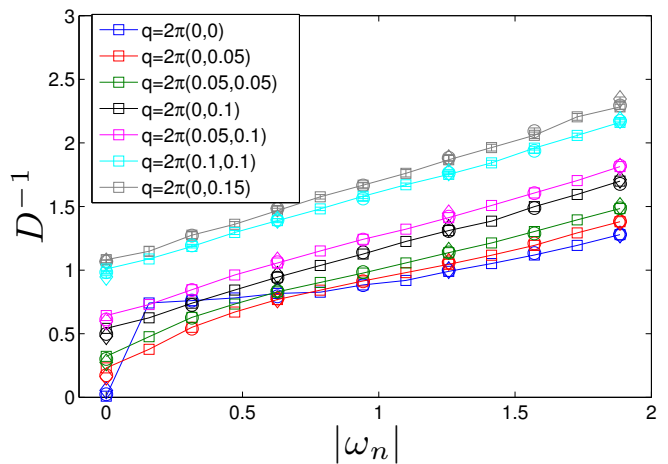


FIG. 9: Frequency dependence of the inverse propagator at  $h = h_c$  for a variety of small momenta  $\mathbf{q}$  in a  $L = 20$  system at temperatures  $T = 0.025, 0.05, 0.1$  (shown as squares, circles, and diamonds respectively). Different colors represent different values of  $\mathbf{q}$ . The frequency dependence is markedly different at  $\mathbf{q} = \mathbf{0}$  and at non-zero  $\mathbf{q}$ . While the curve with  $\mathbf{q} = \mathbf{0}$  is markedly different, the  $\omega_n$  dependence of the remaining curves is similar and roughly linear.

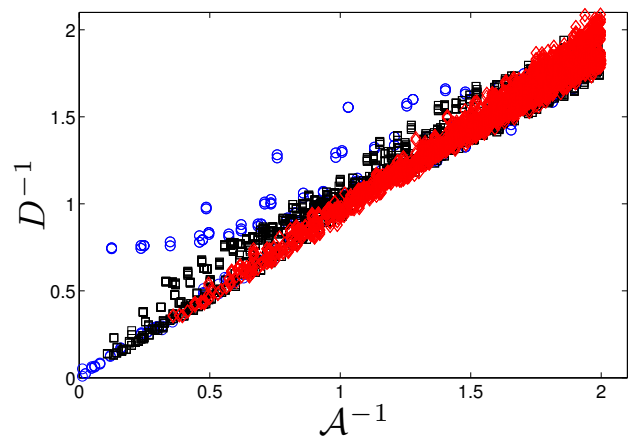


FIG. 10: Comparison between the full dynamical functional approximant,  $\mathcal{A}$  from Eq. 2, and the nematic correlator,  $D$ . Data shown represent  $L = 16, 20$ , and  $24$ ,  $h = 3.525, 3.7, 3.9$ , and  $4.1$ , and temperatures  $T = 1.0, 0.67, 0.5, 0.33, 0.25, 0.17, 0.13, 0.1, 0.05$ , and  $0.025$ . To exhibit the momentum dependence we have used blue circles for  $\mathbf{q} = \mathbf{0}$  (403 data points), black squares for  $|\mathbf{q}| = (2\pi/L)$  and  $(2\pi/L)\sqrt{2}$  (2,840 data points), and red diamonds for all other  $\mathbf{q}$  (5,332 data points).

function of  $|\omega_n|$  with a slope that is independent of  $T$ , and also independent of both the direction and magnitude of  $\mathbf{q}$ . However, at the smallest available non-zero momenta a sublinear dependence on  $|\omega_n|$  is visible. The frequency dependence at  $\mathbf{q} = \mathbf{0}$  is clearly different from the behavior seen for non-zero  $\mathbf{q}$ ; for  $\omega_n \lesssim t$ ,  $D^{-1}(\mathbf{q} = \mathbf{0}, i\omega_n)$  appears to saturate at a frequency independent value, followed by a sudden drop at  $\omega_n = 0$ .

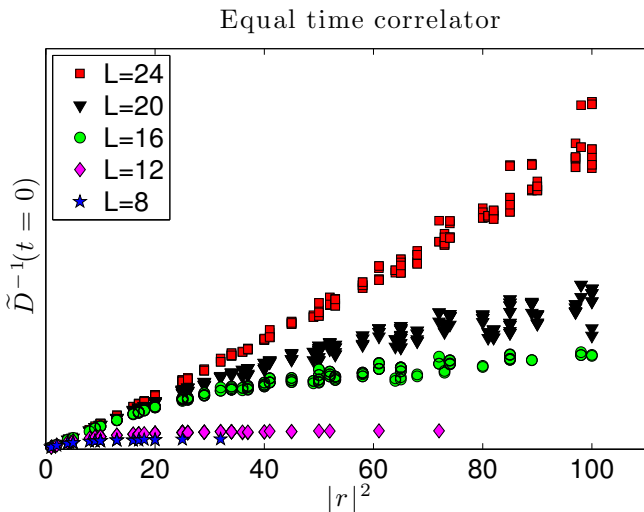


FIG. 11: The inverse of the equal time two-point correlator at  $h = h_c$  and  $T = 0.1$ , plotted versus the square of the spatial separation  $\mathbf{r}$  for various system sizes. The narrow spread in the data (which have not been chosen to lie along any high symmetry direction) indicates an emergent isotropy of the critical correlations in this regime. The trend towards  $1/|\mathbf{r}|^2$  behavior of the propagator in the thermodynamic limit is also clear, consistent with scaling with  $z + \eta \approx 2$ .

To definitively assess the infra-red (IR) dynamics of the model, it is probably necessary to analytically continue to real frequencies, given that even the smallest non-zero Matsubara frequency,  $\omega_1 = 2\pi T$ , is large compared to  $T$ . Methods for doing this exist [68], but they involve subtleties and uncertainties which we have not yet addressed. However, the above cuts through the data show that (with exceptions to be discussed) the data can be well approximated as  $D \approx \mathcal{A}$  from Eq. 2 with  $c = 1.5$  and (as above)  $A \approx 2.1$ ,  $b \approx 2.9t$ , and  $\kappa \approx 2.6t$ .

The validity of this approximation is summarized in Fig. 10. Here we plot  $D^{-1}$  vs  $\mathcal{A}^{-1}$  for system sizes  $L \times L$  with  $L = 16, 20$ , and  $24$ , temperatures  $T/t = 1, 2/3, 1/2, 1/3, 1/4, 1/6, 1/8, 1/10$ , and  $1/20$ ,  $h = h_c = 5.25, 3.7, 3.9$ , and  $4.1$ , all  $\omega_n$  and all  $\mathbf{q}$ . Here, to illustrate the different behavior at the smallest values of  $|\mathbf{q}|$ , we have used blue circles for  $\mathbf{q} = \mathbf{0}$ , black squares for  $|\mathbf{q}| = (2\pi/L)$  and  $(2\pi/L)\sqrt{2}$ , and red diamonds for all other  $\mathbf{q}$ . (Large values of  $|\mathbf{q}|$  and  $|\omega_n|$  correspond to values of  $D^{-1}$  outside the range shown.)

The deviation from linear frequency dependence at the smallest momenta requires some additional comment. Formally, one could justify excluding the smallest momenta in the canonical definition of the thermodynamic limit, in which  $L \rightarrow \infty$  before the small  $|\mathbf{q}|$  behavior is explored. Thus, ideally we would like to focus on a range of  $\mathbf{q}$  such that  $2\pi/L \ll |\mathbf{q}| \ll 2\pi$ . However, given our limited range of system sizes ( $L \leq 24$ ), doing so leaves open the question of whether the true asymptotic behavior emerges only below a small momentum scale,  $|\mathbf{q}| \sim (2\pi)0.1$ . The deviation from linearity in  $\omega_n$

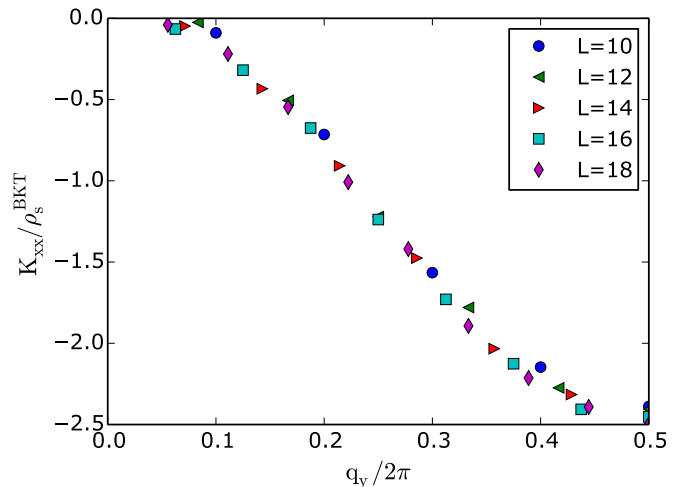


FIG. 12:  $K_{xx}(q_x = 0, q_y)$  defined in Eq. (7) for  $T = 0.05t$ ,  $h = h_c$ , and various values of system size, normalized by the universal value  $\rho_s^{BKT}$ . Momenta from different system sizes lie on the same curve, illustrating the thermodynamic limit. At small values of  $q_y$ ,  $K_{xx}(q_x = 0, q_y)$  lies well below  $\rho_s^{BKT}$ , indicating the system is not superconducting.

in small momenta is particularly apparent at  $\mathbf{q} = \mathbf{0}$ ; we will comment more on this behavior in Sec. IV B below.

Finally, to test the consistency of this analysis, we note that the equal time correlator is the same in both real and imaginary time. Thus, in Fig. 11 we exhibit the inverse of the equal time propagator,  $\tilde{D}(\tau = 0, \mathbf{r})$  for  $h = h_c$  at  $T = 0.1t$ , as a function of distance for various values of  $L$ . Note that for the largest size system ( $L = 24$ ),  $\tilde{D}(0, \mathbf{r}) \sim 1/|\mathbf{r}|^2$ , consistent with what one would get by Fourier transform of  $\mathcal{A}$ . This is also consistent with the general expectation on the basis of a scaling analysis,  $D(0, \mathbf{r}) \sim 1/|\mathbf{r}|^{d+z-2+\eta}$  with  $d = 2$ ,  $z = 2$ , and  $\eta = 0$  and clearly inconsistent with a scaling analysis with, for example,  $z + \eta \approx 3$ . Again, values of  $\tilde{D}$  are shown for all orientations of  $\mathbf{r}$ , so the narrow spread of points gives an impression of the high degree of isotropy exhibited by the data. Note also that for relatively small  $|\mathbf{r}|$ , the data is independent of  $L$ , at least for  $L \geq 16$ , but that at longer distances the data for the smaller systems deviate systematically from the  $|\mathbf{r}|^{-2}$  behavior that appears to characterize the  $L \rightarrow \infty$  limit.

### C. Superconductivity

We have probed for superconducting correlations in the vicinity of the QCP by measuring the superfluid density and the superconducting susceptibility, as a function of  $h$  and  $T$ . The superfluid density is given by [69, 70]

$$\rho_s = \lim_{q_y \rightarrow 0} \lim_{L \rightarrow \infty} K_{xx}(q_x = 0, q_y) \quad (6)$$

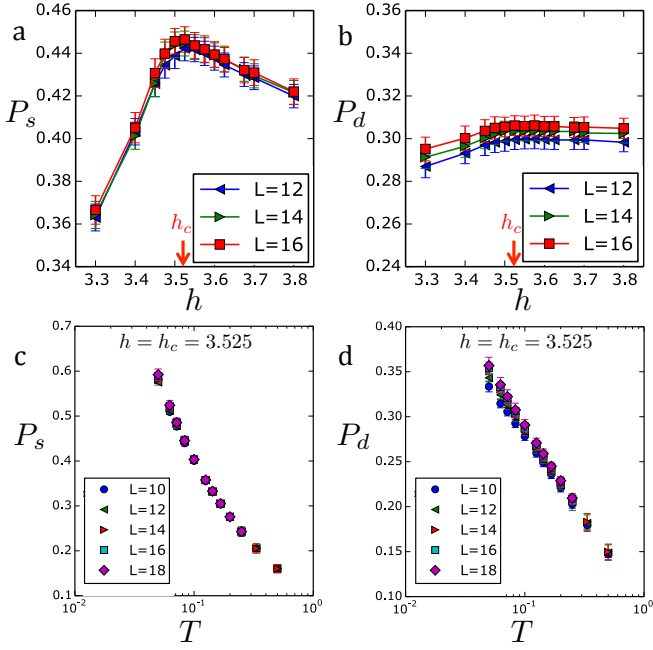


FIG. 13: (a,b) Pairing susceptibility in the  $s$ -wave and  $d$ -wave channels,  $P_{s,d}$  [Eq. (10)], as a function of  $h$ , at  $T = 0.083$ . Different system sizes are displayed. (c,d)  $P_{s,d}$  as a function of temperature at the QCP,  $h = 3.525$ .

where

$$K_{xx}(\mathbf{q}) \equiv \frac{1}{4} [\Lambda_{xx}(q_x \rightarrow 0, q_y = 0) - \Lambda_{xx}(\mathbf{q})], \quad (7)$$

and  $\Lambda_{xx}$  is the current-current correlator

$$\Lambda_{xx}(\mathbf{q}) = \sum_i \int_0^\beta d\tau e^{-i\mathbf{q}\cdot\mathbf{r}_i} \langle j_x(\mathbf{r}_i, \tau) j_x(0, 0) \rangle. \quad (8)$$

Here, the current density operator is given by  $j_x(\mathbf{r}_i) = \sum_\sigma it(1 + \alpha\tau_{i,j}^z) c_{i\sigma}^\dagger c_{j\sigma} + \text{H.c.}$ , where  $\mathbf{r}_j = \mathbf{r}_i + \hat{x}$ .  $K_{xx}(\mathbf{q})$  describes the response of the system to a static orbital magnetic field  $B(\mathbf{q})$ :

$$j_x(\mathbf{q}) = -4K_{xx}(\mathbf{q})A_x(\mathbf{q}), \quad (9)$$

where  $A_x(\mathbf{q}) = iB(\mathbf{q})/q_y$  is the vector potential in an appropriate gauge.

Extrapolating  $K_{xx}$  to the thermodynamic limit is challenging due to the presence of strong finite-size effects associated with the Fermi surface. These finite size effects are dramatically reduced by performing the computations in the presence of a weak uniform magnetic field [71]. We adopt this procedure, but make the field spin-dependent, with the total flux through the system being  $2\pi$  ( $-2\pi$ ) for spin up (spin down). As shown in Ref. [48], such a procedure does not introduce a sign problem for the Monte Carlo. Moreover, in the limit of large system size, the magnetic field vanishes. (See Appendix A for the implementation of this effective magnetic field in the simulations.)

Fig. 12 shows  $K_{xx}$  as a function of  $q_y$ , for different system sizes at temperature  $T = 0.05$  and  $h = h_c$ . The data collapse onto a single curve that extrapolates to a value near zero in the limit  $q \rightarrow 0$ . The extrapolated value is clearly much below the universal value at the BKT transition,  $\rho_s^{BKT} = 2T/\pi$ . This implies that at  $h = h_c$ , the system is not superconducting down to  $T = 0.05t$ . Similarly, the superfluid density for  $h \neq h_c$  is found to be below  $\rho^{BKT}$  for all  $T \geq 0.05t$ . Note that, from Eq. (7),  $\lim_{q_y \rightarrow 0} K_{xx}/q_y^2$  is the orbital susceptibility. From Fig. 12, we see that in our system, this quantity is negative, hence the orbital response is paramagnetic [72]. This indicates that there are no strong superconducting fluctuations (which would produce diamagnetism).

We have also computed the superconducting susceptibilities in the  $s$ -wave ( $A_{1g}$ ) and  $d$ -wave ( $B_{1g}$ ) channels, as a function of  $h$  and  $T$ :

$$P_{s,d} = \int_0^\beta d\tau \sum_i \langle \Delta_{s,d}^\dagger(\mathbf{r}_i, \tau) \Delta_{s,d}(0, 0) \rangle. \quad (10)$$

Here,  $\Delta_s(\mathbf{r}_i) = c_{i\uparrow}c_{i\downarrow}$  and  $\Delta_d(\mathbf{r}_i) = \sum_j \eta_{ij}(c_{i\uparrow}c_{j\downarrow} - c_{i\downarrow}c_{j\uparrow})$ , where  $\eta_{ij}$  is defined below Eq. (5). The superconducting susceptibilities are displayed in Fig. 13. As expected for a non-superconducting state, both  $P_s$  and  $P_d$  saturate as a function of system size at fixed  $T$  and  $h$  [see Fig. 13(a,b)].  $P_s$  has a maximum at  $h \approx h_c$ , while  $P_d$  is smaller and more or less independent of  $h$ .

The enhancement of  $P_s$  by nematic fluctuations is further reflected in its behavior as a function of temperature at a fixed  $h$  [Fig. 13(c,d)].  $P_s$  rises more rapidly than logarithmically at low temperatures. In contrast for non-interacting electrons  $P \sim \log(T_0/T)$ , a functional form consistent with the  $T$  dependence of  $P_d$  at low  $T$ . We interpret this as an indication that the  $s$ -wave susceptibility is enhanced by induced attractive interactions mediated by nematic fluctuations; the ground state for  $h$  near  $h_c$  is likely an  $s$ -wave superconductor, although with  $T_c < 0.05t$ .

#### D. Single Fermion Correlations

Having found that the system is not superconducting down to the temperatures reached in this study, we examine the single-fermion Green's function to glean information about the metallic state in the vicinity of the QCP. The metal is naturally characterized via the single particle density of states  $N(\omega)$ , the Fermi velocity  $\mathbf{v}_F$ , and the quasiparticle weight  $Z_{\mathbf{k}_F}$ . However, measuring these quantities within DQMC is not straightforward, since they generally require real-frequency information inaccessible without analytic continuation. In addition,  $\mathbf{v}_F$  and  $Z_{\mathbf{k}_F}$  are well defined only at zero temperature, while our simulations are at finite temperature. We partially resolve these difficulties by defining finite temperature objects  $\tilde{N}(T)$ ,  $\mathbf{v}_F(T)$ , and  $Z_{\mathbf{k}_F}(T)$  which can be measured numerically, and whose zero temperature limits

are  $N(\omega = 0)$ ,  $\mathbf{v}_{\mathbf{F}}$ , and  $Z_{\mathbf{k}_{\mathbf{F}}}$  respectively. Readers interested in the raw frequency dependence of the fermionic Green's function and self-energy are referred to appendix D.

Real frequency information can be extracted from our imaginary-time data using the identity [73]:

$$G(\mathbf{k}, \tau > 0) = \int_{-\infty}^{\infty} d\omega \frac{e^{-\omega(\tau - \beta/2)}}{2 \cosh(\beta\omega/2)} A(\mathbf{k}, \omega), \quad (11)$$

where  $A(\mathbf{k}, \omega)$  is the fermion spectral function.  $G(\mathbf{k}, \beta/2)$  is evidently equal to the spectral function integrated over a range of energies  $\sim T$ . We therefore define

$$\begin{aligned} \tilde{N}(T) &\equiv \frac{1}{T} \int \frac{d^2k}{(2\pi)^2} G(\mathbf{k}, \tau = \beta/2) \\ &= \int_{-\infty}^{\infty} \frac{d\omega}{2T \cosh(\beta\omega/2)} N(\omega), \end{aligned} \quad (12)$$

$$\mathbf{v}_{\mathbf{F}}(T) \equiv \frac{\partial^2}{\partial \mathbf{k} \partial \tau} \log [G(\mathbf{k}, \tau)] \Big|_{\mathbf{k}=\mathbf{k}_{\mathbf{F}}, \tau=\beta/2}, \quad (13)$$

$$Z_{\mathbf{k}_{\mathbf{F}}}(T) \equiv 2G(\mathbf{k}_{\mathbf{F}}, \tau = \beta/2). \quad (14)$$

We explain in Appendix C how these quantities attain the desired zero temperature limits. We also discuss in the appendix the procedures used to estimate these quantities in finite size systems with discrete momentum and imaginary time.

Fig. 14 shows  $\tilde{N}(T)$  for an  $L = 20$  system as a function of  $h$ , for different temperatures.  $\tilde{N}(T)$  remains nonzero for all values of  $h$ , consistent with a finite density of states in the limit  $T \rightarrow 0$ . This indicates the absence of a substantial gap in the fermionic spectrum, even a nodal gap, down to  $T = t/12$ , corroborating the conclusion of Sec. III C that the system is not superconducting down to these temperatures. Moreover, the fact that  $\tilde{N}(T)$  seems to neither vanish nor diverge at low temperature and  $h = h_c$  has important implications for the nature of the metallic state of the QCP. Were the fermions to acquire a positive (negative) anomalous dimension,  $\eta_F$ , the density of states would go to zero (diverge) at  $T = 0$  [28, 74]. We elaborate on this point in Sec. IV. Instead, the saturation of the density of states is consistent with a Fermi liquid, at least down to the temperature scales in our simulations. Note, as well, that the density of states appears to be depressed with increasing nematic order for  $h < h_c$ .

The results for  $Z_{\mathbf{k}_{\mathbf{F}}}(\theta, T)$ , where  $\theta$  is the angle between  $\mathbf{k}_{\mathbf{F}}$  and the  $x$  axis, are shown in Fig. 15 for different values of  $h \geq h_c$ . At  $\theta = 45^\circ$ ,  $Z_{\mathbf{k}_{\mathbf{F}}}$  is close to unity at all temperatures. This can be understood as a consequence of the fact that at  $\theta = 45^\circ$ , the coupling between fermions and the nematic critical modes vanishes by symmetry; hence, at these ‘‘cold spots’’, the effects of scattering off the critical modes are minimal.  $Z_{\mathbf{k}_{\mathbf{F}}}$  decreases systematically as

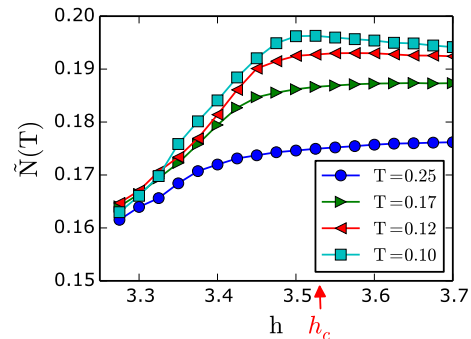


FIG. 14:  $\tilde{N}(T)$ , defined in Eq. (12), as a function of  $h$  for system size  $L = 20$  at different temperatures.  $\tilde{N}$  equals the density of states at the Fermi energy in the limit  $T \rightarrow 0$ .

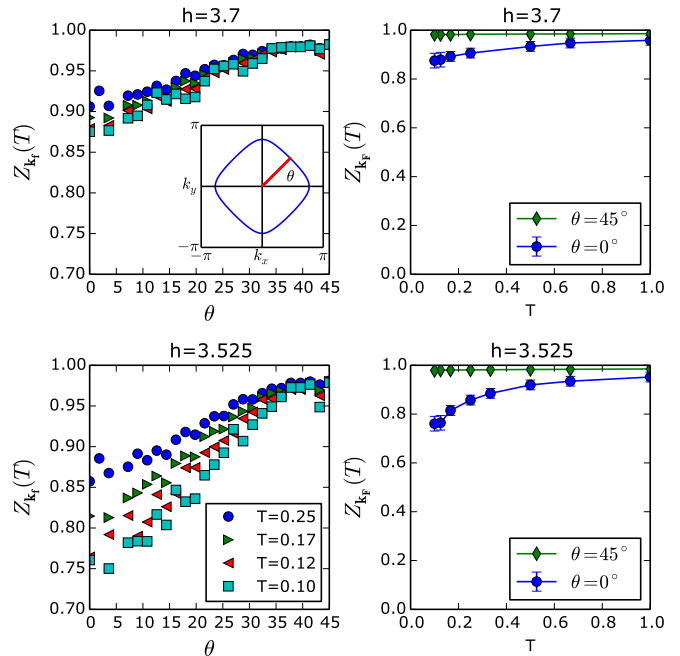


FIG. 15: Left panels show  $Z_{\mathbf{k}_{\mathbf{F}}}$  [defined in Eq. 14] as a function of angle  $\theta$  along the Fermi surface, for different values of  $h$ . The QCP is at  $h_c \approx 3.525$ . Right panels show the temperature dependence of  $Z_{\mathbf{k}_{\mathbf{F}}}(T)$  for high symmetry directions of  $k_{\mathbf{F}}$ .  $Z_{\mathbf{k}_{\mathbf{F}}}$  approaches the conventionally defined quasiparticle weight as  $T \rightarrow 0$ .

$\theta$  approaches  $0^\circ$ , and as  $h$  approaches  $h_c$ .  $Z(k_{\mathbf{F}}, \theta = 0, T)$  decreases with decreasing temperature with negative curvature. On the basis of the present data, it is difficult to say whether it extrapolates to a finite value in the  $T \rightarrow 0$  limit (indicating a FL ground state), or vanishes with a small exponent,  $Z \sim T^{a_Z}$  where  $a_Z \approx 0.1$  (indicating a breakdown of FL behavior). It would be difficult to reconcile the data with  $a_Z$  larger than about 0.15.

Fig. 16(a) shows the same data as a function of  $h \geq h_c$  for  $\theta = 0^\circ$  and  $\theta = 45^\circ$ , emphasizing the decrease in  $Z_{\mathbf{k}_{\mathbf{F}}}$  as  $h$  approaches  $h_c$ . Measuring  $Z_{\mathbf{k}_{\mathbf{F}}}$  close to the QCP for  $h < h_c$  (in the nematic phase) has proven difficult, since



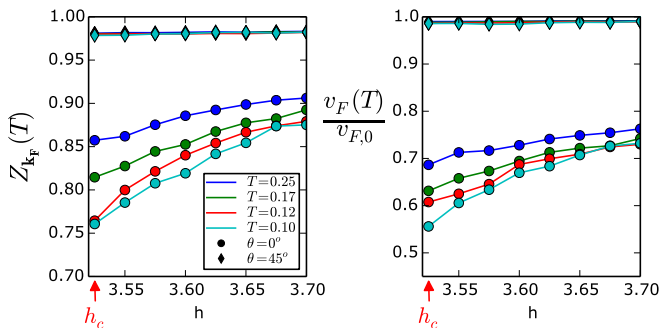


FIG. 16: (a)  $Z_{\mathbf{k}_F}$  as a function of  $h$  for different temperatures. Circles (diamonds) correspond to  $\theta = 45^\circ$  ( $\theta = 0^\circ$ ), respectively (where  $\theta$  is defined in the inset of Fig. 15). (b) The Fermi velocity renormalization,  $v_F/v_{F,0}$  (where  $v_F$  is defined in Eq. 13 and  $v_{F,0}$  is the non-interacting Fermi velocity) as a function of  $h$  for  $\theta = 0^\circ, 45^\circ$ .

the two configurations of the order parameter correspond to two different Fermi surfaces with a small splitting between them. In Fig. 16(b) we show the renormalization of the Fermi velocity,  $v_F/v_{F,0}$ , where  $v_{F,0}$  is the Fermi velocity for the non-interacting band structure ( $\alpha = 0$ ). As with  $Z_{\mathbf{k}_F}$ ,  $v_F$  is hardly renormalized at the cold spot  $\theta = 45^\circ$ . In contrast, at  $\theta = 0^\circ$ ,  $v_F$  is strongly reduced from its non-interacting value, and the velocity renormalization increases as  $h$  approaches  $h_c$ . However, down to  $T = 0.1t$ , there is no obvious indication that  $v_F$  vanishes (i.e., the effective mass diverges) as  $T \rightarrow 0$ , even at  $h = h_c$ .

Over the temperature range explored in this study, the single fermion Green’s function is consistent with a renormalized Fermi liquid, with an angle- and  $h$ -dependent quasi-particle weight and velocity. However, the expected differences between a Fermi liquid and a “marginal Fermi liquid” or a weak (small  $a_Z$ ) non Fermi liquid are subtle at non-zero  $T$ . We can rule out a non-Fermi liquid with a substantial value of  $a_Z$  and/or  $\eta_F$ , but not one with  $a_z$  and  $\eta_F$  sufficiently small.

## IV. DISCUSSION

### A. Comparison with theory

The theory of metallic QCPs, along with the closely related theory of metals coupled to fluctuating gauge fields[75–77], has traditionally been treated by integrating out the fermions to obtain an effective action for the bosonic modes that is highly non-local in both space and time. In this “Hertz-Millis” approach, a renormalization group (RG) analysis is then undertaken for the effective field theory so defined. While much can be learned from this program, there are at least two general causes for concern: 1) The analyticity of the  $\beta$ -function, which is a core ingredient of RG, is typically ensured by the locality of the action. For a non-local action, all aspects

of the analysis, especially the enumeration of potentially relevant interactions that can be generated under RG, need to be tested explicitly. 2) In many cases, including in particular the 2D nematic QCP [67, 78], if one considers the back effect of the collective fluctuations on the fermions, one finds that Fermi liquid theory is perturbatively unstable. The question then arises concerning the self-consistency of the effective action which is obtained by integrating out an assumed Fermi liquid.

Nonetheless, there is a general feeling that this approach is reliable in large enough spatial dimension [79] [103], and its main results are similar in structure to those of many subsequent studies. Accordingly, we briefly review the main features of the Hertz-Millis treatment of the Ising nematic QCP.

In this context, the quadratic part of the effective action for the nematic mode is of the form

$$D_0^{-1}(\mathbf{q}, \omega_n) = r + \kappa|\mathbf{q}|^2 + \alpha^2 Q(\mathbf{q}, \omega_n) \quad (15)$$

where  $r$  and  $\kappa$  are (renormalized) functions of  $T$  and  $h$ , and  $Q$  is the suitably defined particle-hole response function (with the zero-frequency piece subtracted)

$$Q(\mathbf{q}, \omega_n) \equiv \int \frac{d\mathbf{k}}{(2\pi)^2} \frac{i\omega_n |g(\mathbf{k}, \mathbf{q})|^2 [f(\varepsilon_{\mathbf{k}+\mathbf{q}}) - f(\varepsilon_{\mathbf{k}})]}{[\varepsilon_{\mathbf{k}+\mathbf{q}} - \varepsilon_{\mathbf{k}}][i\omega_n + \varepsilon_{\mathbf{k}+\mathbf{q}} - \varepsilon_{\mathbf{k}}]}, \quad (16)$$

where  $g(\mathbf{k}, \mathbf{q})$  is a dimensionless form factor of appropriate symmetry, whose form depends on microscopic details (e.g.  $g(\mathbf{k}, \mathbf{q}) = \cos(k_x) - \cos(k_y)$ ). The essential features of this expression relate to its asymptotic (IR) behavior in the limit  $E_F \gg |\mathbf{v}_F||\mathbf{q}| \gg |\omega_n|$ ,

$$Q(\mathbf{q}, \omega_n) \sim |g(\hat{\mathbf{k}}_{\mathbf{q}}, 0)|^2 \frac{|\omega_n|}{|\mathbf{v}_F||\mathbf{q}|}, \quad (17)$$

where  $\hat{\mathbf{k}}_{\mathbf{q}}$  is the point on the Fermi surface (assumed to be unique mod inversion) at which the Fermi velocity,  $\mathbf{v}_F$ , is perpendicular to  $\mathbf{q}$ . (The fact that the integral in Eq. (16) for given  $\mathbf{q}$  is dominated by the neighborhood of this point on the Fermi surface is the essential observation motivating the “patch” theories of this problem.)

The Hertz-Millis approach implies that the dynamical exponent  $z = 3$  at tree level. From this, a naive scaling analysis (neglecting the possibility of higher-order non-local interactions) concludes that, since  $d + z = 5$  is well above the Ising upper critical dimension, mean-field exponents  $\nu = 1/2$ ,  $\gamma = 1$ , and  $\eta = 0$  apply, consistent with what we find. (See Table I.) Moreover, one would expect violations of scaling (for instance  $\tilde{z} \neq z$  and  $\lambda \neq 1/\nu z$ ). Indeed in Refs. [3, 16, 80, 81] it is shown that at criticality, such an analysis leads to  $r \sim T \log[E_F/T]$ . As we do not have the dynamical range to detect a logarithm, this, too, is consistent with our results.

However, on the face of it, our results for the dynamical response are inconsistent with a dynamical exponent  $z = 3$  and with the sort of anisotropies one might expect from the patch construction. Specifically,  $D^{-1}$  depends roughly linearly on  $|\omega_n|$  with  $\mathbf{q}$  independent coefficient. Moreover, the relative weakness of any deviations

of the single-particle properties from Fermi liquid behavior appears inconsistent with the Hertz-Millis predictions [104]. On the other hand, as we will discuss below, given the somewhat different character of the dynamical correlations at the smallest values of  $|\mathbf{q}|$ , it is also possible that the true asymptotics would only be clear at larger  $L$  and lower  $T$ .

The foregoing discussion of inconsistencies between our data and Hertz-Millis theory can be applied to numerous subsequent attempts to bring the problem under theoretical control. Among the approaches employed by these studies, whose results have similar structure to those of Hertz-Millis, are large  $N_F$  methods (where  $N_F$  is the number of fermion flavors) [17, 20, 21], dimensional [33, 82, 83] and dynamical [18, 19, 30] regularization, and higher dimensional bosonization [84, 85]. The related problem of orbital loop current criticality in a metal has been argued [11, 86] to lead to a critical bosonic propagator with  $|\omega|$  frequency dependence (as seen in our results), but with an asymptotic absence of momentum dependence (not seen in our results) characteristic of “local quantum criticality” [87]. In the vicinity of  $d = 3$ , several varieties of intermediate asymptotics corresponding to different schemes of large  $N_F$  and  $N_B$  (the number of boson flavors) have also been explored [32, 88], at least one of which has  $z = 2$  upon naive extrapolation to  $d = 2$ . We believe our results motivate investigation of possible fixed points involving fermions and a  $z = 2$  boson, and suggest that the isotropy of bosonic correlations we observe should prompt a reexamination of the prevailing “patch” constructions.

Finally, there has been considerable theoretical interest in the issue of superconductivity in the neighborhood of a nematic quantum critical point. It has been argued [36–38, 42] that superconductivity with a critical temperature of order 1 times microscopic scales should be expected near the nematic quantum critical point. Indeed, it has been suggested that the superconducting  $T_c$  at criticality may be so high that it preempts the quantum critical regime in which non-Fermi liquid behavior would be expected. More modestly, in the small  $\alpha$  limit, it has been shown [41] that nematic fluctuations do indeed mediate attractive pairing interactions, and that the resulting transition temperature grows singularly as the quantum critical point is approached either from the ordered or the disordered side. In agreement with this latter result, the superconducting susceptibilities shown in Fig. 13 do show a maximum at  $h = h_c$ . However, if  $T_c$  at criticality is a number of order 1 times the Fermi energy, that number is apparently sufficiently small that  $T_c < E_F/70$  for our chosen parameters.

## B. Caveats

The thermodynamic nematic correlations exhibit a scaling behavior that is broadly consistent with theoretical expectations. In contrast, the apparent  $z = 2$  scaling

of the dynamical correlations, along with the behavior of the fermionic spectral function, are at odds with the theoretical expectations of  $z \approx 3$  and strong deviations from Fermi-liquid behavior. The thermodynamic correlations are well described by the functional approximant,  $\mathcal{A}(\omega_n = 0)$ , so the thermodynamic scaling analysis is straightforward. In contrast, there are clear differences between  $\mathcal{A}$  and the measured correlation function at the smallest wave-numbers and for small but non-zero Matsubara frequencies. It is possible that these differences are finite size effects associated only with wave-numbers such that  $|\mathbf{q}L| \sim 1$ , and thus negligible in the thermodynamic limit. Conversely, they could herald a crossover in the dynamics that would become obvious closer to criticality.

Specifically, the strongest deviation of  $D^{-1}$  from linearity in  $|\omega_n|$  appears at  $\mathbf{q} = \mathbf{0}$  (see Fig. 9). In particular, there is a sharp drop in  $D^{-1}(\mathbf{q} = \mathbf{0})$  at  $\omega_n = 0$ . If this behavior is indeed representative of the thermodynamic limit, it has important physical implications: Fourier transforming to imaginary time, it indicates that the nematic order parameter is very long-lived. This could happen if the order parameter couples to a nearly conserved operator. Such a feature is consistent with Hertz-Millis theory, in which conservation of quadrupole density is inherited from Fermi liquid theory. In contrast, the  $\mathbf{q} \neq \mathbf{0}$  data and the equal-time correlator (Figs. 9, 11) do not agree with Hertz-Millis scaling.

If we are seeing harbingers of a further crossover, then even our largest size systems and lowest temperatures are insufficient to access the universal dynamical critical properties. However, it is plausible that dynamical correlations could be more sensitive to deviations from criticality than thermodynamic ones. While the best way to resolve these issues would be to carry out calculations for much larger systems and lower temperatures, this approach is not promising in the near future. On the other hand, as any crossover scale must depend on non-universal (microscopic) aspects of the problem, universality can be tested by repeating the present calculations for other values of  $V/t$ ,  $\alpha$ , and  $\mu$ .

We have purposely worked with a value of the coupling,  $\alpha = 1/2$ , which is not small. However, because the nematic transition certainly becomes first order for large enough  $\alpha$  [105], we chose a value of  $\alpha < 1$ . There are emergent energy scales in the problem that are parametrically small in the small  $\alpha$  limit, [41] and it is possible that some of these are still small for  $\alpha = 1/2$  [106]. Of particular importance in this regard is the superconducting  $T_c$ . If  $T_c$  depends strongly on  $\alpha$ , increasing of  $\alpha$  from  $\alpha = 1/2$  to  $\alpha = 1$  could produce a measurable value of  $T_c$ ; it is also conceivable that it would produce scaling behavior more in line with the expectations of one theoretical treatment or another.

We have taken the electron density per site to be substantial,  $n = 0.8$ , so that the mean value of  $2k_F = (2\pi)0.71 \gg (2\pi/L)$ . However, there is a small spanning vector  $Q = (2\pi)0.23$  connecting Fermi surface copies in

adjacent Brillouin zones (see Fig. 2), and this might lead to a crossover scale at small momentum.

In the near future, we plan to explore the behavior of the present model for different values of the parameters and especially for larger values of  $\alpha$  and smaller values of the electron density, i.e. for larger values of  $Q$ . Moreover, we estimate that it should be possible – although extremely time consuming – to carry out calculations for system sizes as large as  $L = 30$ .

### C. Relation to experiment

There is increasingly extensive evidence that electron nematic phases are common in highly correlated electronic fluids.[89] In particular, it has been suggested that a nematic QCP occurs near optimal doping in both the cuprates[90, 91] and in the Fe-based superconductors[92, 93]. However, the experimental situation in all these cases is complicated, and in some cases controversial.

It is premature to attempt any sort of serious comparison between the present results and the experiments in these materials. However, the experimental case is clearest in certain Fe based superconductors, so it is worth noting a few points of comparison. Most strikingly, elastoresistance [60, 65], Raman scattering [61, 64], and elastic constant [63] measurements show a large range of  $T$  and doping over which a large nematic susceptibility can be documented with a remarkably systematic Currie Weiss  $T$  dependence  $\chi \sim 1/[T - T^*(x)]$  where  $T^*(x)$  appears to depend roughly linearly on “doping” concentration,  $x$ , and to pass through zero at a critical doping concentration,  $x_c$ , which approximately coincides with the optimal doping for superconductivity. [107] It is impossible not to be encouraged by the similarity between this experimental finding and our numerical results.

### Acknowledgments

We are grateful to D. Chowdhury, A. Chubukov, S. Hartnoll, R. Fernandes, E. Fradkin, A. Millis, S. Raghu, and S. Sachdev for illuminating discussions. E. B. and Y. S. were supported by the ISF under grant 1291/12, by the US-Israel BSF, and by a Marie Curie CIG grant. SAK was supported in part by NSF grant #DMR 1265593 at Stanford. SL was supported, in part by DOE, grant # DE-AC02-76SF00515, an ABB Fellowship at Stanford, and a Gordon and Betty Moore Post Doctoral Fellowship at MIT.

## Appendix A: Technical details of the DQMC simulations

Discretizing imaginary time as  $\beta = N\Delta\tau$ , the grand partition function becomes

$$\Xi = \text{Tr}_{\{\tau\}} \text{Tr}_{\{c,c^\dagger\}} \prod_{n=1}^{N/2} \left( \hat{B} \hat{B}^\dagger \right) + O(\Delta\tau^2), \quad (\text{A1})$$

where

$$\hat{B} = e^{-\frac{\Delta\tau}{2} H_h} e^{-\Delta\tau H_V} e^{-\Delta\tau H_\mu} \prod_{m=1}^4 \left( e^{-\Delta\tau c^\dagger K^{(m)} c} \right) e^{-\frac{\Delta\tau}{2} H_h}. \quad (\text{A2})$$

Here,  $c^\dagger = (c_{1,\uparrow}^\dagger, c_{1,\downarrow}^\dagger, c_{2,\uparrow}^\dagger, c_{2,\downarrow}^\dagger, \dots)$  is a row vector of spin 1/2 fermionic creation operators for the spatial sites  $1, 2, \dots, L^2$ , where  $L$  is the linear dimension.  $H_h, H_V$ , and  $H_\mu$  are the terms in Eq. 4 proportional to  $h, V$ , and  $\mu$  respectively. We use a checkerboard decomposition to describe the kinetic energy matrices  $K^{(m)}$ , whose elements are  $K_{i,j,\sigma,\sigma'}^{(m)} = -t_{i,j}^{(m)}(\sigma)(1 - \alpha\tau_{i,j}^z)\delta_{\sigma,\sigma'}$ , i.e.,  $m = 1, 2, 3, 4$  enumerates the horizontal/vertical bonds originating from a site with an even/odd index. We allow  $t_{i,j}$  to depend on spin in order to implement the spin-dependent magnetic field discussed below.

Plugging in unity operators in the  $\tau_{ij}$  sector at every time slice and taking the trace over the fermions, we bring the partition function to a form which can be sampled using Monte-Carlo techniques:

$$\Xi = \sum_{\{\tau_{i,j;n} = \pm 1\}} e^{-S_\tau} \det \left( 1 + e^{\beta\mu} \prod_{n=1}^{N/2} T_{2n-1} T_{2n}^\dagger \right) + O(\Delta\tau^2), \quad (\text{A3})$$

where  $T_n = \prod_{m=1}^4 \left( e^{-\Delta\tau K_n^{(m)}} \right)$  is a matrix which depends implicitly on the c-numbers  $\tau_{i,j;n} = \pm 1$  through the relation  $K_{i,j,\sigma,\sigma';n}^{(m)} = -t_{i,j}^{(m)}(\sigma)(1 - \alpha\tau_{i,j;n})\delta_{\sigma,\sigma'}$ , and the bosonic part of the action is given by

$$S_\tau = \frac{1}{2} \log(\tanh(\Delta\tau h)) \sum_{\langle i,j \rangle, n} \tau_{i,j;n} \tau_{i,j;n+1} + V\Delta\tau \sum_{\langle\langle i,j;k,l \rangle\rangle, n} \tau_{i,j;n} \tau_{k,l;n}. \quad (\text{A4})$$

We have used  $\Delta\tau = 0.05$  in our simulations.

Monte-Carlo sampling is most efficient when the determinant in (A3) is positive. Here, the absence of a sign problem is guaranteed by microscopic time reversal symmetry. To see this, note that the matrices  $T_n$  are block diagonal in the spin sector, and so the total determinant is the product of the spin up and spin down determinants. If time reversal is preserved, i.e.

$$t_{i,j}(\uparrow) = t_{i,j}^*(\downarrow), \quad (\text{A5})$$

then the product of the determinants is clearly positive.

It has long been known[71] that finite size effects in fermionic systems, in particular at low temperatures, can be greatly improved by the application of a weak orbital magnetic field. On a finite size system with periodic boundary conditions, the field must be such that an integer multiple of the flux quantum passes through the system,  $\Phi = n\Phi_0$ . In order to preserve time reversal symmetry as required in (A5), in this work we have applied the opposite field for both spin species, such that  $\Phi_\uparrow = -\Phi_\downarrow = \Phi_0$ . Such a field vanishes in the thermodynamic limit.

Although our simulations do not suffer from the sign problem, close to the quantum critical point our simulations do suffer from critical slowing down. To avert this, we found it was helpful to include global Monte-Carlo updates, in addition to local (Metropolis) ones. Our global updates consisted of a slight modification to the Wolff algorithm[94]: Starting from a space-time configuration of pseudo-spins, a cluster of pseudo-spins is constructed using the usual Wolff algorithm, supposing our action is given by (A4), i.e without taking into account the coupling to the fermions. Next, we propose flipping the pseudo-spins which belong to the cluster, and accept the move with a probability which is the ratio of the determinants in (A3) between the two configurations. It can easily be seen that such a move obeys detailed balance.

### Appendix B: Finite size scaling analysis

The finite temperature phase boundary  $T_N(h)$  (or equivalently  $h_N(T)$ ) can be computed by using *classical* finite size scaling techniques for two dimensional Ising transitions, characterized by susceptibility exponent  $\gamma = 7/4$  and correlation length exponent  $\nu = 1$ . At a given temperature and for a given system size  $L$ , the most singular part of the thermodynamic susceptibility,  $\chi_s$ , satisfies

$$\chi_s(h; L) = L^{\gamma/\nu} F((h - h_N) L^{1/\nu}) \quad (\text{B1})$$

$h_N$  can therefore be identified by a single parameter data collapse, as illustrated in Fig. 17. At low temperatures, the region of parameter space corresponding to classical criticality narrows, so that larger system sizes are needed to reliably estimate  $h_N$ .

### Appendix C: Characterizing the metallic state

Write the imaginary time Green's function in a spectral representation:

$$\begin{aligned} G(\mathbf{k}, \tau > 0) &= \langle c_{\mathbf{k}}(\tau) c_{\mathbf{k}}^\dagger(0) \rangle \\ &= \sum_{m,n} \frac{e^{-\beta \varepsilon_n}}{\Xi} e^{\tau(\varepsilon_n - \varepsilon_m)} |\langle n | c_{\mathbf{k}} | m \rangle|^2. \end{aligned} \quad (\text{C1})$$

Here,  $|n\rangle$  is a many-body eigenstate with energy  $\varepsilon_n$ , and  $\Xi$  is the grand partition function. In this representation,

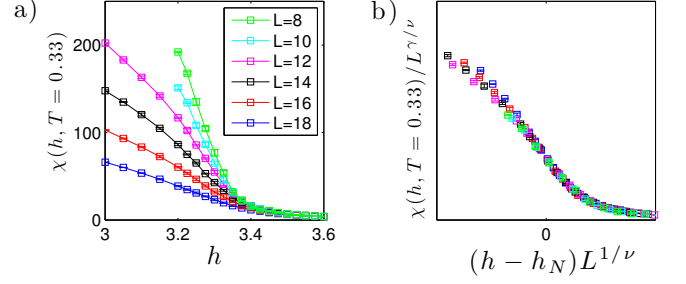


FIG. 17: An example of the procedure used to calculate the critical value of  $h$  for a given temperature. Here, for  $T = 0.33$ , the best data collapse is obtained for  $h_N \approx 3.27$ . The exponents take the two dimensional Ising values  $\gamma = 7/4, \nu = 1$  for this thermal transition.

the fermion spectral function is

$$A(\mathbf{k}, \omega) = \sum_{m,n} \frac{e^{-\beta \varepsilon_n} + e^{-\beta \varepsilon_m}}{\Xi} |\langle n | c_{\mathbf{k}} | m \rangle|^2 \delta(\omega + \varepsilon_n - \varepsilon_m), \quad (\text{C2})$$

we can write Eq. (C1) as [73]

$$G(\mathbf{k}, \tau > 0) = \int_{-\infty}^{\infty} d\omega \frac{e^{-\omega(\tau - \beta/2)}}{2 \cosh(\beta\omega/2)} A(\mathbf{k}, \omega). \quad (\text{C3})$$

If the ground state is a Fermi liquid, we can extract the quasi-particle weight and Fermi velocity renormalization from Eq. (C3). We assume that at low temperatures, the spectral function in the vicinity of the Fermi surface obtains a Fermi liquid form,  $A(\mathbf{k}, \omega) = A_{\text{qp}}(\mathbf{k}, \omega) + A_{\text{reg}}(\mathbf{k}, \omega)$ , where  $A_{\text{qp}}$  is the quasi-particle contribution and  $A_{\text{reg}}(\mathbf{k}, \omega)$  is a regular background. In the limit  $T \rightarrow 0$ ,  $A_{\text{qp}}$  becomes a delta-function like peak:  $A_{\text{qp}} \approx Z_{\mathbf{k}_F} \delta(\omega - \varepsilon_{\mathbf{k}})$ , where  $\varepsilon_{\mathbf{k}} = \mathbf{v}_F \cdot (\mathbf{k} - \mathbf{k}_F)$  is the quasi-particle dispersion near the Fermi surface,  $Z_{\mathbf{k}_F}$  is the quasi-particle weight,  $\mathbf{v}_F$  is the Fermi velocity. At finite but small  $T$  and  $\varepsilon_{\mathbf{k}}$ , the quasi-particle peak at  $\mathbf{k}_F$  obtains a width that scales as  $\max(T^2, \varepsilon_{\mathbf{k}}^2)$ . The regular part satisfies  $A_{\text{reg}}(\mathbf{k}, \omega) = O[\max(T^2, \omega^2, \varepsilon_{\mathbf{k}}^2)]$ .

Inserting the Fermi liquid form of  $A(\mathbf{k}, \omega)$  into Eq. (C3), we obtain that at low temperatures,

$$G(\mathbf{k}, \tau > 0) \approx \frac{Z_{\mathbf{k}_F} e^{-\varepsilon_{\mathbf{k}}(\tau - \beta/2)}}{2 \cosh(\beta \varepsilon_{\mathbf{k}}/2)}. \quad (\text{C4})$$

We can use this relation to estimate  $Z_{\mathbf{k}_F}$  and  $v_{\mathbf{k}_F}$  along the Fermi surface. For a point on the Fermi surface,  $Z_{\mathbf{k}_F} = 2G(\mathbf{k}_F, \beta/2)$ . The dispersion can be estimated from  $\varepsilon_{\mathbf{k}} = -d \log[G(\mathbf{k}, \tau)]/d\tau|_{\tau=\beta/2}$ , and the Fermi velocity is then evaluated according to  $v_{\mathbf{k}} = \nabla_{\mathbf{k}} \varepsilon_{\mathbf{k}}$ . Some caution is needed because in our finite size systems, the values of  $\mathbf{k}$  are quantized, and the  $\mathbf{k}$  grid does not in general intersect the Fermi surface. One can instead estimate  $Z_{\mathbf{k}}$  from the points nearest to the Fermi surface. Also, our measurements of  $G(\mathbf{k}, \tau)$  are taken at finite temperatures, yielding the finite temperature estimators  $\tilde{N}(T)$ ,  $\mathbf{v}_F(T)$ ,



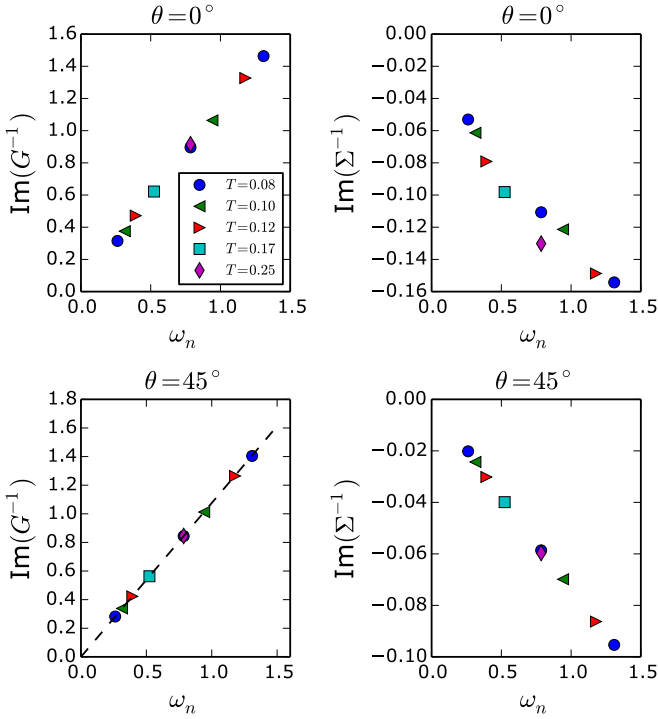


FIG. 18: Left panels: The imaginary part of the inverse of the Matsubara Green's function  $\text{Im}(G^{-1}(\mathbf{k}_F, \omega_n))$  for  $h = 3.525$ . Data points from different temperatures mostly lie on the same curve. Right panels: The imaginary part of the self energy. The dashed line in the bottom left panel corresponds to  $Z = 0.93$ .

and  $Z_{\mathbf{k}_F}(T)$  discussed in the text (Equations 12, 13, and 14). An extrapolation to the limit  $T \rightarrow 0$  is necessary in order to deduce the “true” Fermi liquid properties, to the extent they are well defined.

#### Appendix D: Fermion Green's function and self-energy

In Fig. 18 we show the Matsubara frequency dependence of the inverse fermion Green's function. Linear frequency dependence, consistent with a Fermi liquid, seems to dominate down to the lowest frequencies available. Finer details are visible by considering the self energy (right panels) which shows both a noticeable temperature dependence and a deviation from linearity for  $\theta = 0^\circ$ .

- 
- [1] E. Fradkin and S. A. Kivelson, *Nature Physics* **8**, 864 (2012).
- [2] J. A. Hertz, *Physical Review B* **14**, 1165 (1976).
- [3] A. J. Millis, *Phys. Rev. B* **48**, 7183 (1993).
- [4] R. B. Laughlin, G. G. Lonzarich, P. Monthoux, and D. Pines, *Advances in Physics* **50**, 361 (2001), <http://dx.doi.org/10.1080/00018730110098534>.
- [5] P. Gegenwart, Q. Si, and F. Steglich, *Nature Physics* **4**, 186 (2008).
- [6] A. Rost, S. Grigera, J. Bruin, R. Perry, D. Tian, S. Raghu, S. A. Kivelson, and A. Mackenzie, *Proceedings of the National Academy of Sciences* **108**, 16549 (2011).
- [7] A. J. Millis, A. J. Schofield, G. G. Lonzarich, and S. A. Grigera, *Phys. Rev. Lett.* **88**, 217204 (2002).
- [8] Selected recent developments regarding quantum critical behavior in these material families include Refs. [95] and [96] in cuprates, and Refs. [97] and [65] in Fe-based superconductors.
- [9] P. A. Lee, *Phys. Rev. Lett.* **63**, 680 (1989).
- [10] C. Castellani, C. Di Castro, and M. Grilli, *Zeitschrift für Physik B Condensed Matter* **103**, 137 (1996).
- [11] C. M. Varma, *Phys. Rev. B* **55**, 14554 (1997).
- [12] A. Rosch, *Phys. Rev. Lett.* **82**, 4280 (1999).
- [13] L. Dell'Anna and W. Metzner, *Phys. Rev. Lett.* **98**, 136402 (2007).
- [14] D. L. Maslov, V. I. Yudson, and A. V. Chubukov, *Phys. Rev. Lett.* **106**, 106403 (2011).
- [15] V. Barzykin and D. Pines, *Phys. Rev. Lett.* **96**, 247002 (2006).
- [16] S. A. Hartnoll, R. Mahajan, M. Punk, and S. Sachdev, *Phys. Rev. B* **89**, 155130 (2014).
- [17] B. Altshuler, L. Ioffe, and A. Millis, *Physical Review B* **50**, 14048 (1994).
- [18] C. Nayak and F. Wilczek, *Nuclear Physics B* **430**, 534 (1994).
- [19] C. Nayak and F. Wilczek, *Nuclear Physics B* **417**, 359 (1994).
- [20] B. L. Altshuler, L. B. Ioffe, and A. J. Millis, *Phys. Rev. B* **52**, 5563 (1995).
- [21] A. Abanov and A. V. Chubukov, *Phys. Rev. Lett.* **83**, 1652 (1999).
- [22] A. Abanov and A. Chubukov, *Physical review letters* **84**, 5608 (2000).
- [23] A. Abanov, A. Chubukov, and J. Schmalian, *Advances in Physics* **52**, 119 (2003).
- [24] A. Abanov and A. Chubukov, *Physical Review Letters* **93**, 255702 (2004).
- [25] M. J. Lawler, D. G. Barci, V. Fernández, E. Fradkin, and L. Oxman, *Phys. Rev. B* **73**, 085101 (2006).
- [26] H. v. Löhneysen, A. Rosch, M. Vojta, and P. Wölfle, *Rev. Mod. Phys.* **79**, 1015 (2007).



- [27] S.-S. Lee, *Phys. Rev. B* **80**, 165102 (2009).
- [28] M. Metlitski and S. Sachdev, *Physical Review B* **82**, 075127 (2010).
- [29] M. Metlitski and S. Sachdev, *Physical Review B* **82**, 075128 (2010).
- [30] D. F. Mross, J. McGreevy, H. Liu, and T. Senthil, *Physical Review B* **82**, 045121 (2010).
- [31] D. L. Maslov and A. V. Chubukov, *Phys. Rev. B* **81**, 045110 (2010).
- [32] A. L. Fitzpatrick, S. Kachru, J. Kaplan, and S. Raghu, *Phys. Rev. B* **88**, 125116 (2013).
- [33] D. Dalidovich and S.-S. Lee, *Phys. Rev. B* **88**, 245106 (2013).
- [34] T. Holder and W. Metzner, *Phys. Rev. B* **92**, 041112 (2015), [arXiv:1503.05089 \[cond-mat.str-el\]](#) .
- [35] A. J. Millis, *Phys. Rev. B* **45**, 13047 (1992).
- [36] A. Abanov, A. V. Chubukov, and A. M. Finkel'stein, *EPL (Europhysics Letters)* **54**, 488 (2001), [cond-mat/9911445](#) .
- [37] R. Roussev and A. Millis, *Physical Review B* **63**, 140504 (2001).
- [38] M. A. Metlitski and S. Sachdev, *New Journal of Physics* **12**, 105007 (2010).
- [39] Y. Wang and A. V. Chubukov, *Phys. Rev. Lett.* **110**, 127001 (2013).
- [40] T. Maier and D. J. Scalapino, (2014), [arXiv:1405.5238](#) .
- [41] S. Lederer, Y. Schattner, E. Berg, and S. A. Kivelson, *Physical review letters* **114**, 097001 (2015).
- [42] M. A. Metlitski, D. F. Mross, S. Sachdev, and T. Senthil, *Physical Review B* **91**, 115111 (2015).
- [43] M. Einenkel, H. Meier, C. Pépin, and K. B. Efetov, *Phys. Rev. B* **91**, 064507 (2015).
- [44] K. B. Efetov, H. Meier, and C. Pépin, *ArXiv e-prints* (2012), [arXiv:1210.3276 \[cond-mat.str-el\]](#) .
- [45] Y. Wang and A. Chubukov, *Phys. Rev. B* **90**, 035149 (2014).
- [46] R. Blankenbecler, D. J. Scalapino, and R. L. Sugar, *Physical Review D* **24**, 2278 (1981).
- [47] F. F. Assaad, "Quantum Simulations of Complex Many-Body Systems: From Theory to Algorithms" (Lecture Notes), published in: J. Grotendorst, D. Marx, A. Muramatsu (Eds.), *John von Neumann Institute for Computing*, Julich, pp. 99-156 (2002).
- [48] C. Wu and S.-C. Zhang, *Physical Review B* **71**, 155115 (2005).
- [49] E. Berg, M. A. Metlitski, and S. Sachdev, *SCIENCE* **338**, 1606 (2012).
- [50] Z.-X. Li, Y.-F. Jiang, and H. Yao, *Phys. Rev. B* **91**, 241117 (2015).
- [51] F. F. Assaad and I. F. Herbut, *Physical Review X* **3**, 031010 (2013), [arXiv:1304.6340 \[cond-mat.str-el\]](#) .
- [52] Z.-X. Li, Y.-F. Jiang, and H. Yao, *ArXiv e-prints* (2014), [arXiv:1411.7383 \[cond-mat.str-el\]](#) .
- [53] L. Wang, P. Corboz, and M. Troyer, *New Journal of Physics* **16**, 103008 (2014), [arXiv:1407.0029 \[cond-mat.str-el\]](#) .
- [54] R. A. Borzi, S. A. Grigera, J. Farrell, R. S. Perry, S. J. S. Lister, S. L. Lee, D. A. Tennant, Y. Maeno, and A. P. Mackenzie, *Science* **315**, 214 (2007).
- [55] V. Hinkov, D. Haug, B. Fauqué, P. Bourges, Y. Sidis, A. Ivanov, C. Bernhard, C. T. Lin, and B. Keimer, *Science* **319**, 597 (2008).
- [56] R. Daou, J. Chang, D. LeBoeuf, O. Cyr-Choinière, F. Laliberté, N. Doiron-Leyraud, B. J. Ramshaw, R. Liang, D. A. Bonn, W. N. Hardy, and L. Taillefer, *Nature* **463**, 519 (2010).
- [57] M. Lawler, K. Fujita, J. Lee, A. Schmidt, Y. Kohsaka, C. K. Kim, H. Eisaki, S. Uchida, J. Davis, J. Sethna, *et al.*, *Nature* **466**, 347 (2010).
- [58] C.-L. Song, Y.-L. Wang, P. Cheng, Y.-P. Jiang, W. Li, T. Zhang, Z. Li, K. He, L. Wang, J.-F. Jia, *et al.*, *Science* **332**, 1410 (2011).
- [59] S. C. Riggs, M. C. Shapiro, A. V. Maharaj, S. Raghu, E. D. Bauer, R. E. Baumbach, P. Giraldo-Gallo, M. Wartenbe, and I. R. Fisher, *Nature Communications* **6**, 6425 (2015), [arXiv:1405.7403 \[cond-mat.str-el\]](#) .
- [60] J.-H. Chu, H.-H. Kuo, J. G. Analytis, and I. R. Fisher, *Science* **337**, 710 (2012), [arXiv:1203.3239 \[cond-mat.supr-con\]](#) .
- [61] Y. Gallais, R. M. Fernandes, I. Paul, L. Chauvière, Y.-X. Yang, M.-A. Méasson, M. Cazayous, A. Sacuto, D. Colson, and A. Forget, *Phys. Rev. Lett.* **111**, 267001 (2013).
- [62] R. Zhou, Z. Li, J. Yang, D. Sun, C. Lin, and G.-q. Zheng, *Nature communications* **4** (2013).
- [63] A. E. Böhmer, P. Burger, F. Hardy, T. Wolf, P. Schweiss, R. Fromknecht, M. Reinecker, W. Schranz, and C. Meingast, *Physical Review Letters* **112**, 047001 (2014), [arXiv:1305.3515 \[cond-mat.supr-con\]](#) .
- [64] V. K. Thorsmølle, M. Khodas, Z. P. Yin, C. Zhang, S. V. Carr, P. Dai, and G. Blumberg, *ArXiv e-prints* (2014), [arXiv:1410.6456 \[cond-mat.supr-con\]](#) .
- [65] H.-H. Kuo, J.-H. Chu, S. A. Kivelson, and I. R. Fisher, *ArXiv e-prints* (2015), [arXiv:1503.00402 \[cond-mat.supr-con\]](#) .
- [66] C. Varma, P. B. Littlewood, S. Schmitt-Rink, E. Abrahams, and A. Ruckenstein, *Physical Review Letters* **63**, 1996 (1989).
- [67] W. Metzner, D. Rohe, and S. Andergassen, *Phys. Rev. Lett.* **91**, 066402 (2003).
- [68] J. Gubernatis, M. Jarrell, R. Silver, and D. Sivia, *Physical Review B* **44**, 6011 (1991).
- [69] D. J. Scalapino, S. R. White, and S. Zhang, *Physical Review B* **47**, 7995 (1993).
- [70] T. Paiva, R. R. dos Santos, R. T. Scalettar, and P. J. H. Denteneer, *Phys. Rev. B* **69**, 184501 (2004).
- [71] F. F. Assaad, *Phys. Rev. B* **65**, 115104 (2002).
- [72] The paramagnetic sign of the orbital susceptibility is probably a band structure effect. For example, in a non-interacting tight-binding model on a square lattice, the orbital susceptibility is paramagnetic in a range of densities near half filling. Near the band bottom (or top), it becomes diamagnetic.
- [73] N. Trivedi and M. Randeria, *Phys. Rev. Lett.* **75**, 312 (1995).
- [74] T. Senthil, *Phys. Rev. B* **78**, 035103 (2008).
- [75] T. Holstein, R. E. Norton, and P. Pincus, *Phys. Rev. B* **8**, 2649 (1973).
- [76] M. Y. Reizer, *Phys. Rev. B* **40**, 11571 (1989).
- [77] B. I. Halperin, P. A. Lee, and N. Read, *Phys. Rev. B* **47**, 7312 (1993).
- [78] V. Oganesyan, S. A. Kivelson, and E. Fradkin, *Phys. Rev. B* **64**, 195109 (2001).
- [79] S. Sachdev, *Quantum phase transitions* (Wiley Online Library, 2007).
- [80] P. Jakubczyk, P. Strack, A. A. Katanin, and W. Met-

- zner, *Phys. Rev. B* **77**, 195120 (2008).
- [81] J. Bauer, P. Jakubczyk, and W. Metzner, *Phys. Rev. B* **84**, 075122 (2011).
- [82] S. Chakravarty, R. E. Norton, and O. F. Syljuåsen, *Phys. Rev. Lett.* **74**, 1423 (1995).
- [83] T. Senthil and R. Shankar, *Phys. Rev. Lett.* **102**, 046406 (2009).
- [84] M. J. Lawler, D. G. Barci, V. Fernández, E. Fradkin, and L. Oxman, *Phys. Rev. B* **73**, 085101 (2006).
- [85] M. J. Lawler and E. Fradkin, *Phys. Rev. B* **75**, 033304 (2007).
- [86] C. M. Varma, *Phys. Rev. Lett.* **83**, 3538 (1999).
- [87] Q. Si, S. Rabello, K. Ingersent, and J. L. Smith, *Nature* **413**, 804 (2001).
- [88] A. L. Fitzpatrick, S. Kachru, J. Kaplan, and S. Raghu, *Phys. Rev. B* **89**, 165114 (2014), [arXiv:1312.3321 \[cond-mat.str-el\]](https://arxiv.org/abs/1312.3321).
- [89] E. Fradkin, S. A. Kivelson, M. J. Lawler, J. P. Eisenstein, and A. P. MacKenzie, *Annual Review of Condensed Matter Physics* **1**, 153 (2010), [arXiv:0910.4166 \[cond-mat.str-el\]](https://arxiv.org/abs/0910.4166).
- [90] S. A. Kivelson, E. Fradkin, and V. J. Emery, *Nature* **393**, 550 (1998).
- [91] L. Nie, G. Tarjus, and S. A. Kivelson, *Proceedings of the National Academy of Sciences* **111**, 7980 (2014).
- [92] C. Fang, H. Yao, W.-F. Tsai, J. Hu, and S. A. Kivelson, *Physical Review B* **77**, 224509 (2008).
- [93] C. Xu, M. Müller, and S. Sachdev, *Physical Review B* **78**, 020501 (2008).
- [94] U. Wolff, *Phys. Rev. Lett.* **62**, 361 (1989).
- [95] B. J. Ramshaw, S. E. Sebastian, R. D. McDonald, J. Day, B. S. Tan, Z. Zhu, J. B. Betts, R. Liang, D. A. Bonn, W. N. Hardy, and N. Harrison, *Science* **348**, 317 (2015), [arXiv:1409.3990 \[cond-mat.supr-con\]](https://arxiv.org/abs/1409.3990).
- [96] K. Fujita, C. K. Kim, I. Lee, J. Lee, M. H. Hamidian, I. A. Firmo, S. Mukhopadhyay, H. Eisaki, S. Uchida, M. J. Lawler, E.-A. Kim, and J. C. Davis, *Science* **344**, 612 (2014), <http://www.sciencemag.org/content/344/6184/612.full.pdf>.
- [97] K. Hashimoto, K. Cho, T. Shibauchi, S. Kasahara, Y. Mizukami, R. Katsumata, Y. Tsuruhara, T. Terashima, H. Ikeda, M. Tanatar, *et al.*, *Science* **336**, 1554 (2012).
- [98] S. Chakravarty and A. J. Leggett, *Phys. Rev. Lett.* **52**, 5 (1984).
- [99] P. W. Anderson, G. Yuval, and D. Hamann, *Physical Review B* **1**, 4464 (1970).
- [100] R. M. Fernandes, A. V. Chubukov, J. Knolle, I. Eremin, and J. Schmalian, *Phys. Rev. B* **85**, 024534 (2012).
- [101] R. M. Fernandes, S. Maiti, P. Wölfle, and A. V. Chubukov, *Phys. Rev. Lett.* **111**, 057001 (2013).
- [102] While most theoretical treatments have concluded that  $z = 3$ , a dynamical exponent  $z = d$ , possibly as an intermediate asymptotic, is suggested in Ref. [88].
- [103] In  $d = 0$  as well, the Kondo problem can be mapped [98] to the problem of a two-level system coupled to an Ohmic heat bath, for which the non-local effective action is equivalent to that of a  $d = 1$  classical inverse-square Ising model. This problem can, in turn, be treated using a suitable RG analysis [99].
- [104] To our knowledge, the temperature dependence of the quantity  $Z(T)$  defined here has not been explicitly computed within the Hertz-Millis approach. Applying  $\omega/T$  scaling to the  $T = 0$  self energy (which, of course may not be valid) yields  $Z(T) \sim T^{1/3}$ , a noticeably more rapid variation than the data of Fig. 15d.
- [105] See [100] and [101] for a discussion of first order behavior for a magnetically mediated scenario for nematicity in the Fe-based superconductors.
- [106] It is also worth noting that, for sufficiently weak Yukawa coupling, the breakdown of the Fermi liquid description occurs at a scale parametrically smaller than that at which the boson is qualitatively renormalized. Our simulations are performed at substantial Yukawa coupling, but it is nonetheless conceivable that bosonic properties reflect the true IR behavior but fermionic properties do not, over the scales accessible to us.
- [107] Note that this behavior applies in the range of temperatures larger than  $T_c$  and, for  $x < x_c$ , larger than the structural transition temperature,  $T_s$ ; it is to be expected that if the experiments for  $x < x_c$  could be extended down to temperatures approaching sufficiently close to  $T^*(x)$ , somewhat different classical critical behavior would take over.